

Review

Correlative Raman imaging and scanning electron microscopy for advanced functional materials characterization

Fuxi Liu,¹ Xu Zou,¹ Nailin Yue,¹ Wei Zhang,^{1,*} and Weitao Zheng¹

SUMMARY

Confocal Raman imaging and scanning electron (RISE) microscopy, when combined in a microscope, complement each other and provide the emerging opportunities to clarify morphological, structural, and chemical information of materials at the micron and even nanoscale. Specifically, such advanced RISE microscopy enables the elucidations of one region of interest from a perspective of multiple characterization methods rather than the routine sample-based analysis, representing a major leap in comprehensively characterizing samples. Herein, we summarize the principle, development history, and typical application cases of the state-of-the-art technique, ranging from energy storage, catalysis, and environmental science to other various research fields. A promising future of RISE microscopy is highly expected in physical science, particularly in characterizing advanced functional materials.

INTRODUCTION

The Raman effect, a phenomenon in which the frequency of monochromatic light changes with the medium molecules that induce scattering, was first experimentally verified by the Indian physicist C.V. Raman in 1928.¹ Due to the weak Raman effect and the lack of a suitable strong light source, Raman spectroscopy did not develop rapidly until the discovery of the laser in 1961. Raman spectrum analysis does not require complex sample preparation process. Solid, gas, and even liquid samples can all be tested, and no damage occurs for the tested samples; it also holds several other advantages, e.g., a simple procedure, short determination time, and high sensitivity. Since Raman active vibration corresponds to the change of molecular polarizability, each substance has its featured Raman spectrum. Consequently, it can be used to analyze and identify the molecular constitution and the structural and electronic information of different substances. Furthermore, the stress-strain state, crystallinity, defects, and relative concentration of specific components of the tested samples can be qualitatively measured,^{2,3} which has attracted intense interest indeed.^{4–6} Therefore, the relevant Raman techniques have witnessed a rapid development into different types,⁷ such as confocal Raman spectroscopy,⁸ *in situ* Raman spectroscopy,^{9–13} surface-enhanced Raman spectroscopy,^{14–16} resonant Raman spectroscopy,¹⁷ and Fourier transform Raman spectroscopy.¹⁸ Compared with the single Raman technique, the correlative Raman characterization technique is superior. For example, very high detection sensitivity can be obtained by using surface-enhanced Raman spectroscopy. As the detection sensitivity of a single molecule level can be afforded for some specific systems, the interference of fluorescence can be effectively avoided in experiments.

However, the traditional Raman spectroscopy techniques suffer from certain disadvantages, e.g., small depth of field, poor contrast, low spatial resolution, etc. It can

¹Key Laboratory of Automobile Materials MOE, and School of Materials Science & Engineering, and Jilin Provincial International Cooperation Key Laboratory of High-Efficiency Clean Energy Materials, and Electron Microscopy Center, and International Center of Future Science, Jilin University, Changchun 130012, Jilin, China

*Correspondence: weizhang@jlu.edu.cn

<https://doi.org/10.1016/j.xcpr.2023.101607>



only obtain the molecular composition and structural and electronic information of a material; unfortunately, the topographical and morphological information is inaccessible yet crucial in the same region of interest for the tested samples. Fortunately, scanning electron microscopy (SEM) can well compensate for the small depth of field and low spatial resolution of Raman microscopy, achieving high-resolution surface morphological images. SEM has two basic and commonly used signals, secondary electron (SE) and back-scattered electron (BSE). SE reflects mainly morphology-based contrast, whereas BSE represents composition-based as well as some morphology-based contrast. When observing the morphology of samples via SEM, it is necessary to select the appropriate signal. For instance, if the conductivity of a material is insufficient, a charging effect or a localized charge will occur, and BSE imaging is less affected compared with SE imaging. In addition, for the samples with very flat surfaces without obvious morphology contrast, one can perform channel contrast imaging via BSE. Overall, although SEM can probe the surface topography and morphology, there are limitations in acquiring other certain information. To overcome the limitations, SEM is thereof combined with other analytical techniques to obtain complementary information for the concerned materials, such as energy-dispersive X-ray spectroscopy (EDS)-SEM, soft X-ray emission spectroscopy (SXES)-SEM,^{19–21} atomic force microscopy-SEM,²² focused ion beam (FIB)-SEM,^{23,24} time-of-flight secondary ion mass spectrometry (TOF-SIMS)-FIB-SEM,²⁵ etc. The joint use of different complementary characterization techniques can provide more comprehensive information about the tested samples, which is of great significance in the analysis and characterization of materials. For instance, SXES, which can afford information on the local structure and the electronic properties of materials with a very high energy resolution (0.3 eV) and detection limit (20 ppm), can be attached to a SEM to simultaneously obtain high-resolution morphology images. In addition, elemental analysis plays an important role in microanalysis. Conventional elemental characterization methods (EDS or wavelength-dispersive X-ray spectroscopy [WDS]) are less powerful for the analysis of light elements, whereas TOF-SIMS probes any element starting from H with a high limit of detection. TOF-SIMS coupled with FIB-SEM enables the concurrent acquisition of sample morphology and elemental information just in the same region, allowing for the 3D analysis of the elements of interest assisted by FIB etching. For instance, TOF-SIMS-FIB-SEM has been widely used in Li-ion batteries. Sun et al. demonstrated by using this technique that the MXenes coating on a LiCoO₂ can effectively mitigate the decomposition of electrolyte and thereof prevent the excessive accumulation of cathode-electrolyte interphase film at the interface. Thus, the structural stability is largely improved in the cycling process.²⁶

In 2014, WITec and TESCAN developed Raman imaging and scanning electron (RISE) microscopy by combining SEM and confocal Raman microscopy (CRM) in one instrument. Different from the previous two separate systems of SEM and Raman, such an integrated system appears more advanced as well as being equipped with unique confocal function.²⁷ For transparent multilayer film samples, the confocal setup of CRM can be utilized to obtain Raman spectra for the positions with different depths by moving the objective up and down, ultimately offering a true 3D visualization. In short, this is an emerging powerful tool toward an integrated characterization of morphological, chemical, and molecular information of materials at one region of interest.

In this minireview, we summarize the principle of Raman and the development of a correlative SEM-Raman system and showcase the typical application of such RISE microscopy in different fields. On this basis, the advantages of the RISE system,

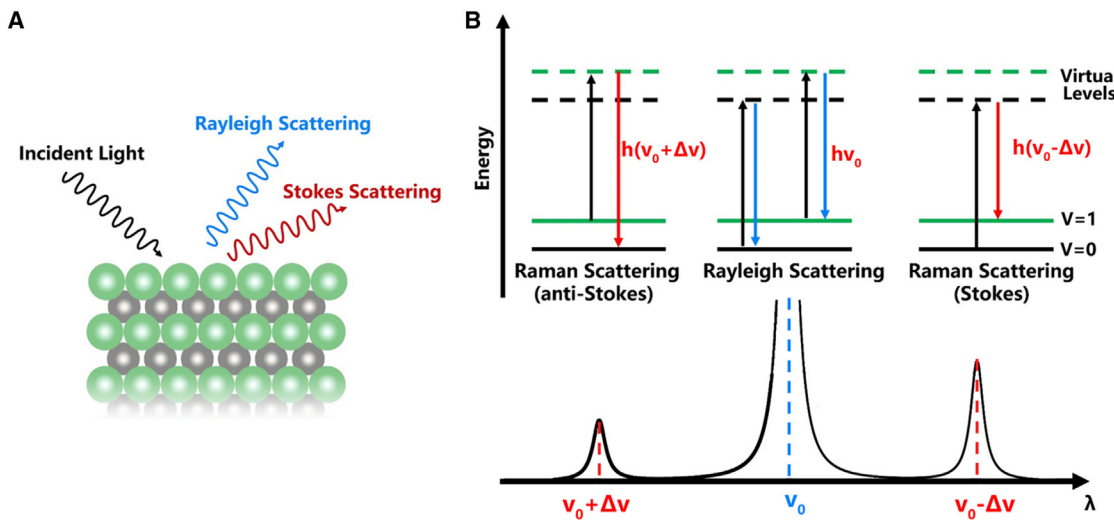


Figure 1. The detection principle of Raman spectrum

(A) Schematic diagram of Raman scattering.
(B) Schematic diagram of energy levels and scattering lines of Raman scattering.

comprising two complementary techniques, are highlighted. Finally, we put forward a prospect for the potential development of the hyphenate system in the field of catalysis. Thus, it is expected to stimulate wide interest to fully utilize this technique for elucidating advanced functional materials.

FUNDAMENTAL AND DEVELOPMENT OF RISE MICROSCOPY

In 1923, the physicist Smekal predicted Raman scattering of light by molecules for the first time through classical quantum theory. Since Indian physicist C.V. Raman verified the Raman scattering effect in 1928, Raman spectrum has gradually become one of the major means to pinpoint molecular structure.¹

The detection principle of Raman spectrum is shown in Figure 1. When a beam of monochromatic light illuminates a transparent sample, the photons collide with the molecules, and the partial incident light is randomly scattered on the surface of the sample (Figure 1A).²⁸ When the photons and molecules have inelastic collision, Raman scattering is generated. Molecules in the ground state of vibration are excited to a higher unstable energy state under the action of photons. In order to maintain the whole system in a stable state, molecules in the high-energy state will spontaneously return to the vibrationally excited state at a low-energy level, where Stokes scattering is generated (Figure 1B).^{29,30} In the case of Raman scattering, the transition probability of Stokes and anti-Stokes lines is equal. Molecules are mostly located at the ground state of vibration at room temperature. Thus, the signal of the Stokes scattering band is stronger, and the Stokes line is mostly used in Raman spectral analysis. The frequency shift of Raman scattered light corresponds to the change of molecular vibration energy levels. Different chemical bonds or groups have different vibration modes, where the corresponding Raman shift provides the finger-print information of molecular vibration.

After continuous development and improvement, Raman spectroscopy can not only obtain the chemical and structural information of materials but can also determine the information of the different vibration modes within the molecules, the crystallinity of materials, and the stress-strain distribution.^{31,32} However, the shortcomings

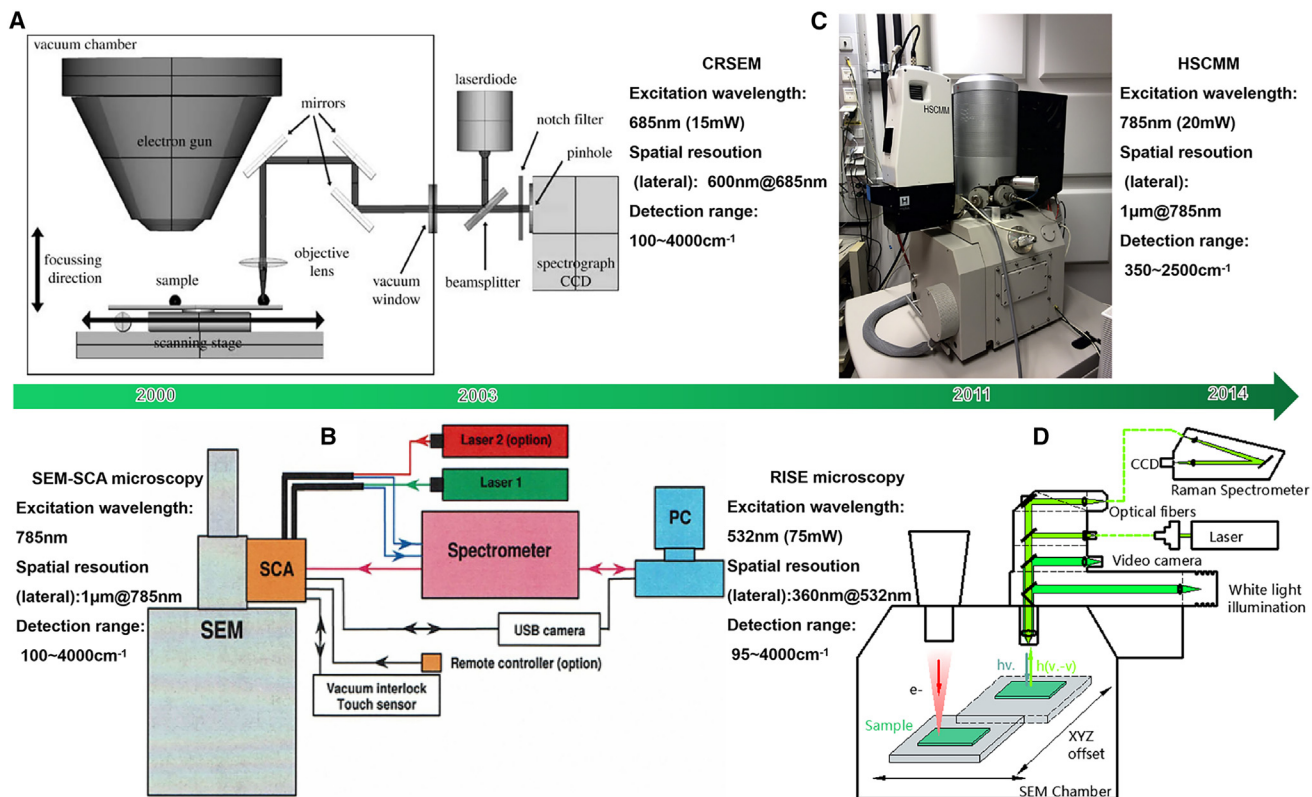


Figure 2. The development of the SEM-Raman system

(A-D) The structural diagrams of CRSEM, SEM-SCA microscopy, HSCMM, and RISE microscopy, respectively. Reproduced with permission.³³ Copyright The Royal Society, 2005. Reproduced with permission.³⁴ Copyright Elsevier, 2016. Reproduced with permission.³⁵ Copyright AIP Publishing, 2015.

of small depth, poor contrast, and low spatial resolution lead to a limitation in analyzing materials. Considering the advantages of SEM with large depth of field and high spatial resolution, scientists innovatively combined SEM and Raman in the process of material characterization to simultaneously obtain information on the morphology and molecular composition of samples. The development for a SEM-Raman system is shown in Figure 2.

In 2000, Aksenov et al. developed a non-commercial, self-built simple hyphenate system for studying the morphology, chemical composition, and molecular composition of biomaterials by combining CRM and SEM (CRSEM) for the first time (Figure 2A). When using 685 nm laser excitation, the system allows for a practical lateral resolution of ~600 nm with an effective laser power (~15 mW on sample).^{33,36,37} Since then, some similar systems have been developed. In 2003, a Renishaw Raman microscope and SEM were integrated, and the SEM structural and chemical analyzer (SEM-SCA) microscope was developed (Figure 2B).^{38,34} In 2011, Hybriscan, based in the Netherlands, entered into a strategic partnership with JEOL and FEI to launch an “off-axis” system-based Raman-SEM microscope system, named the Hybriscan Molecular Microscope (HSCMM) (Figure 2C).^{34,35,39} Later, the world’s first truly practical SEM-Raman hyphenate system was designed (Figure 2D).

In 2014, WITec (Germany) collaborated with TESCAN (Czech Republic) to combine SEM and CRM, pioneering a new type of the completely integrated correlation

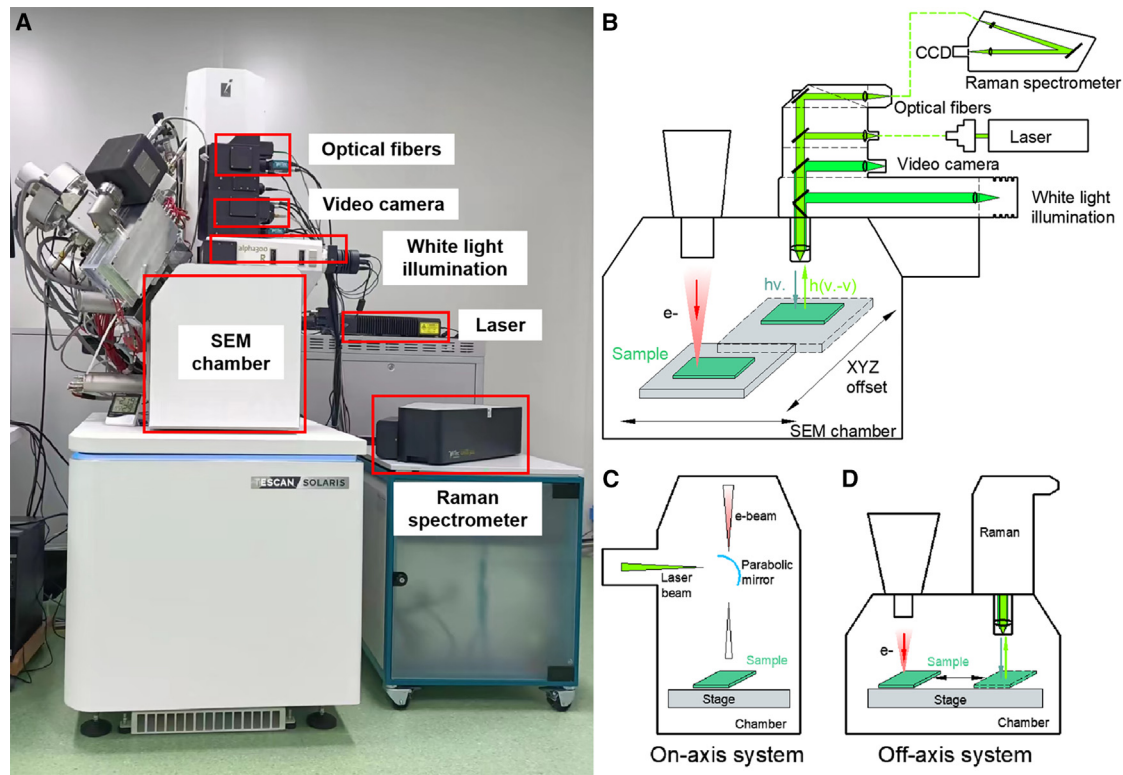


Figure 3. Photo and schematic diagram of RISE microscopy

(A) RISE microscopy integrates a SEM and a CRM within a single instrument; photo from the Electron Microscopy Center of Jilin University.

(B) Schematic diagram of RISE microscopy.

(C and D) The schematic diagram of SEM-Raman systems based on the “on-axis” and “off-axis” principles, respectively.

microscopy technique, and thus developed commercial RISE microscopy, as shown in Figures 3A and 3B. In this system, the objective lens of the Raman microscope and the electron gun of the SEM are parallel to each other. Unlike the “on-axis” system (Figure 3C), the RISE microscope based on an “off-axis” system can effectively avoid the optical compromise of an optical microscope (Figure 3D).²⁷ Different from the previous SEM and Raman systems, the interference problem of integrated SEM and Raman is completely avoided and achieves a resolution comparable to that of independent instruments. When using 532 nm laser excitation, the confocal setup of the Raman microscope can provide 360 nm lateral resolution with an effective laser power of 75 mW.⁴⁰ Moreover, the confocal setup not only reduces the backside and improves the quality of the Raman spectrum and the resolution of Raman imaging but also allows more new and expanded analysis work for different samples. As a result, it enables capturing two sets of data: a single Raman spectrum at the specified sample location and SEM-confocal Raman imaging on the same instrument. The collected SEM images and Raman optical images were superimposed and fitted using software that comes with RISE microscopy to visualize the morphological information of the sample in the Raman imaging region. In addition to 2D Raman imaging, this system can also carry out 3D confocal Raman imaging and can conduct lossless 3D tomography analysis of laser-transmittable samples.⁴¹ The sample region of interest is first observed morphologically in the window of a SEM, and then the sample stage is precisely moved to the position of the CRM and repositioned automatically through the accurate control of the software. Thus, the same sample region can be analyzed chemically and structurally in the window of the

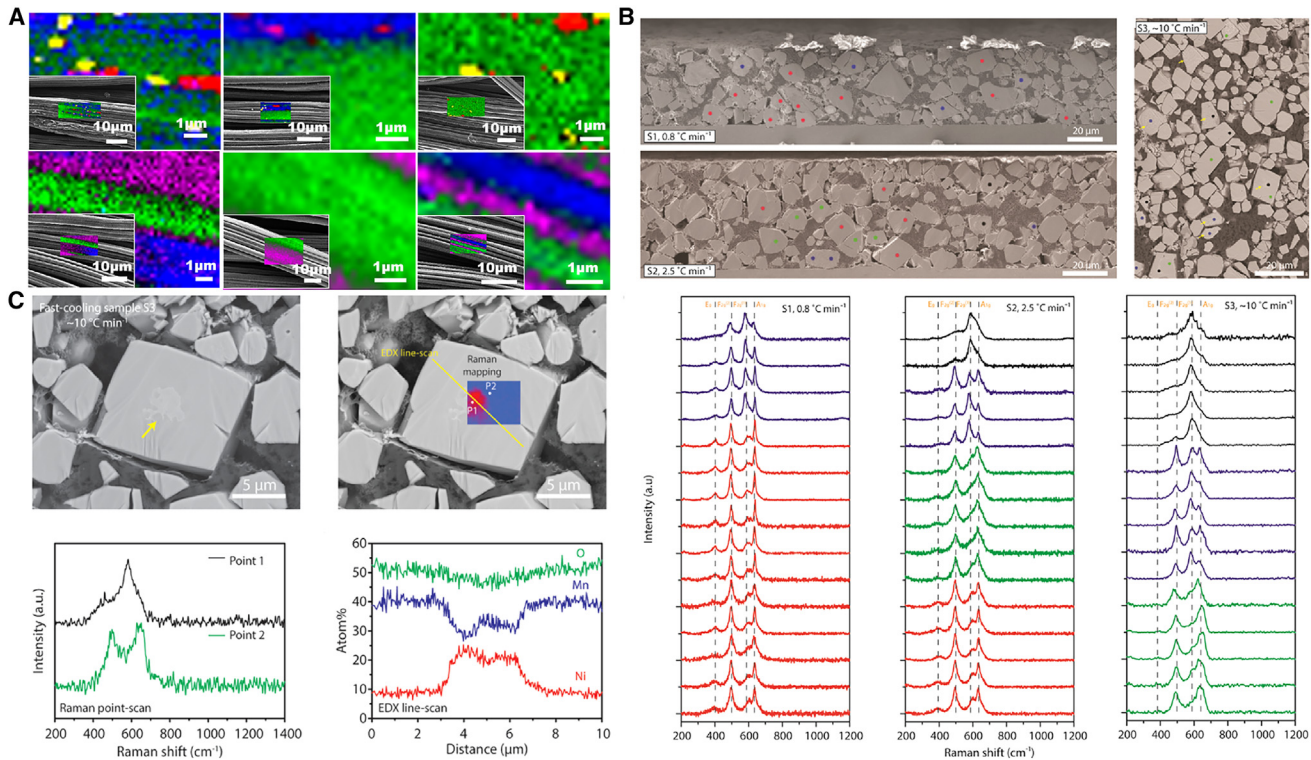


Figure 4. SEM images, Raman spectra, and RISE mappings of CFC, BC6-Ni1-K6, and LNMO

(A) RISE images of CFC, 350CFC, 400CFC, 425CFC, 450CFC, and 475CFC, respectively. Reproduced with permission.⁴⁵ Copyright Elsevier, 2020.

(B) Cross-sectional SEM images of LNMO samples at different cooling rates, and Raman spectra of the corresponding samples. Reproduced with permission.⁴⁹ Copyright American Chemical Society, 2020.

(C) Cross-sectional SEM image of a rapidly cooled (~10°C/min) LNMO particle, as well as Raman mapping, Raman spectra, and EDS line analysis at this location. Reproduced with permission.⁴⁹ Copyright American Chemical Society, 2020.

CRM. Therefore, it is possible to obtain high-resolution images as well as chemical and structural information in the same region of the sample.

APPLICATIONS OF RISE MICROSCOPY

The application in energy storage

In recent years, RISE microscopy has become more and more popular because it can offer the morphology, molecular composition, and phase structural information of materials in the same region of interest concurrently.^{42–44}

In 2019, Zheng et al. explored the relationship between the electrochemical properties of carbon fiber cloth (CFC) and the degree of disorder caused by annealing activation using RISE microscopy.⁴⁵ Samples activated at different annealing temperatures were labeled as 350CFC, 400CFC, 425CFC, 450CFC, and 475CFC, respectively. Through SEM images, one can only observe the obvious changes in the surface morphology of the annealed CFCs. By stacking and fitting Raman images and SEM images, more information can be obtained as shown in Figure 4A, where the red, blue, green, purple, and yellow regions represent a high G/D ratio region, a medium G/D ratio region, a low G/D ratio region, and a fluorescence region, respectively. It can be visualized from Figure 4A that there are fewer red areas and more green areas in the original CFC, the 350CFC, and the 400CFC, confirming the existence of amorphous carbon and edge defects on the surface.⁴⁶ There are no red regions in 425CFC, 450CFC, and 475CFC and are relatively many blue regions, indicating that annealing increases the degree

of disorder of CFC. The fitting image of the 450°C annealed CFC is mainly composed of green regions, and there are no red or blue regions, indicating that 450CFC has a high degree of disorder and that the distribution is relatively uniform. Combined with the Brunauer-Emmett-Teller method, the relationship between the electrochemical performance and the structure of CFC after annealing at different temperatures is demonstrated. In addition, Li et al. studied the reuse process of Ni-coated biochar using the technique and analyzed the hybridization of carbon atoms around nickel particles combined with EDS. Through this system, it visually proved that nickel with a moderate concentration can accelerate the erosion of a carbon layer and promote the formation of an aromatic structure, thus explaining why the electrical double-layer capacitor prepared from biochar-adsorbed Ni^{2+} enhanced its conductivity and stability in the electrochemical testing process.⁴⁷ In 2022, Huang et al. also used this hyphenate system to explore whether there exist other phases in the compound formed by Mo substituting W in CoWO_4 . It well demonstrated that the synthesized intermetallic compound is still the CoWO_4 phase and that no other new phases were formed.⁴⁸

As the positive electrode material of lithium-ion batteries, $\text{LiNi}_{0.5}\text{Mn}_{1.5}\text{O}_4$ (LNMO) still confronts great challenges in the synthesis of pure phase. When the temperature is above 750°C, the ordered phase transforms into a disordered phase and an impurity phase with a rock salt structure.^{50–53} RISE microscopy can obtain the distribution information of the disordered phase and the impurity phase in LNMO well, which is of great significance for the synthesis of materials with phase transformation in the preparation. In 2020, Wang et al. used it for the first time to analyze the transformation process of halite's impurity phase into a spinel phase at different cooling rates at the single-grain level during LNMO preparation to reveal the correlation between structure and electrochemical performance.⁴⁹ Combined with previous studies, it can be seen that red and green spectra are the characteristic features of ordered and disordered phases, respectively, but black spectrum was not mentioned in previous studies (Figure 4B).⁵⁴ Raman mapping was performed on the grain where the black spectrum is located, and the distribution regions of the black and green spectra can be directly seen from Figure 4C. Combined with EDS, it is concluded that the black spectrum is the impurity phase with a nickel-rich rock salt structure. It confirms that slow cooling is crucial to improve the structural order and electrochemical performance of LNMO. It is impossible to obtain information of changes in the internal structure of grains by conventional bulk analysis technique, and the aforementioned information cannot be obtained by using a single CRM. RISE microscopy plays a key role in this study, offering the possibility to study the relationship between the changes in the internal phase structure of grains and the cooling rate.

In 2021, Qian et al. made an in-depth analysis of the influence of crystal defects of $\text{LiNi}_{0.5}\text{Co}_{0.2}\text{Mn}_{0.3}\text{O}_2$ (NMC), the positive electrode material for commercial lithium-ion batteries, on the performance of the hyphenate system.⁵⁵ According to the RISE microregion analysis, Fe-/Cr-based impurities will affect the degree of surface reconstruction and induce partial discharge of NMC particles, directly leading to the capacity attenuation and the polarization increase. Li et al. also analyzed the phase structure of Mo_2CT_x MXene lithium-ion anode material pre-intercalated with NH_4^+ by using RISE microscopy, proving the successful pre-intercalation of NH_4^+ and the successful etching of Ga atoms in $\text{Mo}_2\text{Ga}_2\text{C}$ powder.⁵⁶

In addition to lithium-ion batteries, sodium-ion batteries, magnesium-ion batteries, and dual-ion batteries with high energy density, low cost, and environmental friendliness have also attracted great interest in recent years. Sun et al. further demonstrated with the system that O3-type $\text{NaNi}_{1/3}\text{Fe}_{1/3}\text{Mn}_{1/3}\text{O}_2$ (NFM) loses sodium

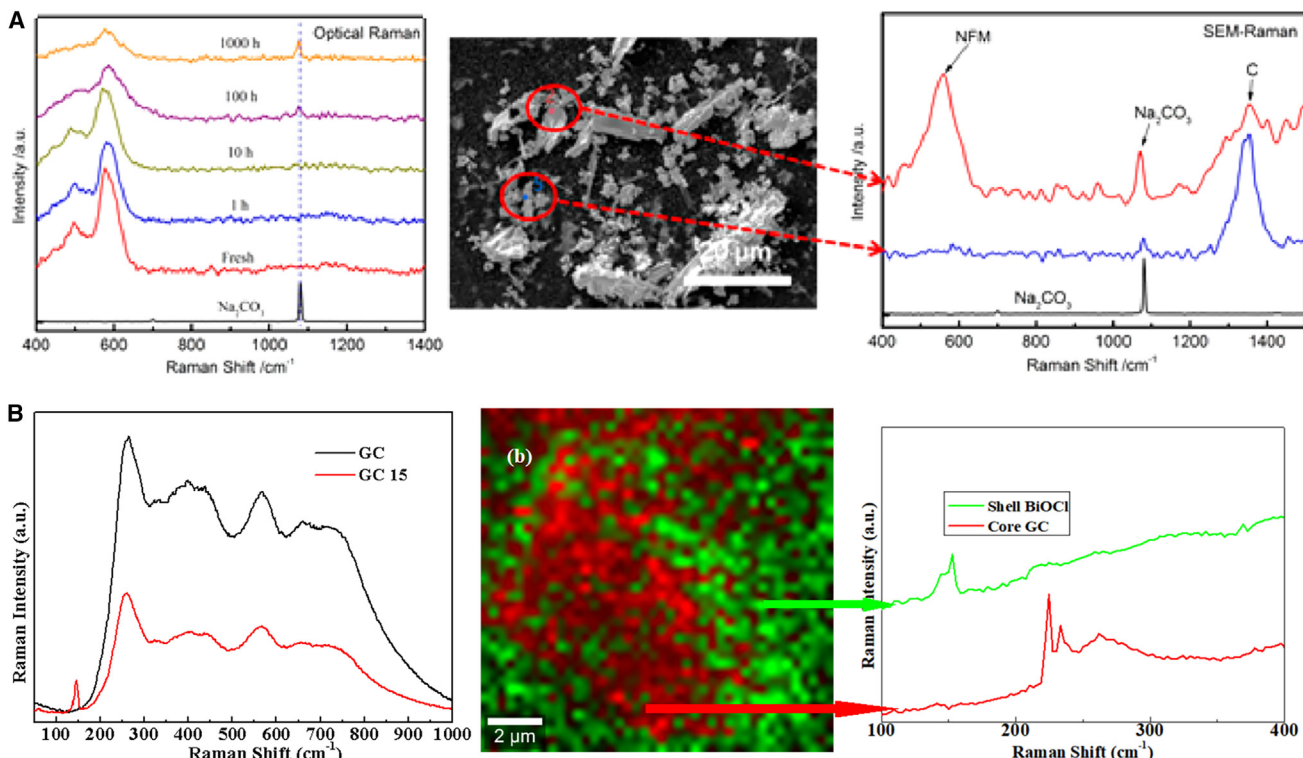


Figure 5. SEM image, Raman spectra, and RISE imaging of NFM and GC

(A) Raman spectra of NFM samples stored in the ambient for different times and SEM images of NFM particles stored for 1,000 h. Reproduced with permission.⁵⁷ Copyright American Chemical Society, 2021.

(B) Raman spectra of GC and GC15 as well as RISE imaging of GC15. Reproduced with permission.⁶⁰ Copyright Elsevier, 2020.

ions during ambient storage and forms sodium carbonate fibers from the surface of NFM particles, resulting in severe capacity loss, which is incomparable to single SEM and X-ray diffraction (XRD) characterization techniques (Figure 5A).⁵⁷ In 2022, Pan et al. used Mn₃O₄ activated by an Na₂SO₄ electrolyte for the first time as the cathode material for an aqueous Mg²⁺ battery, and by combining RISE microscopy, XRD, and transmission electron microscopy (TEM), they revealed the new reaction mechanism of spinel Mn₃O₄ in a drainage battery system.⁵⁸ Through the morphology and phase structure analysis of the microregion of interest conducted by this hyphenate system, it was found that the crystallinity of Mn₃O₄ after activation treatment was reduced, and the part was transformed into an amorphous structure, which was also confirmed by high-resolution TEM images and XRD. At the same time, the morphology changed obviously, and some flocculence or pores were produced. Combined with electrochemical tests, the amorphous-grain refinement structure induced by the Na₂SO₄ electrolyte pre-treatment is conducive to the diffusion of Mg²⁺ and the enhancement of electrochemical capacity, so the manganese tetroxide cathode exhibits excellent performance. In the same year, Yang et al. used RISE microscopy to prove that the graphite structure defects of Li⁺ pre-intercalated carbon paper increased and the degree of graphitization decreased, explaining that Li⁺ pre-intercalated carbon paper promoted the anion diffusion process.⁵⁹

The application in catalysis

The application of RISE microscopy in the field of catalysis is more inclined to phase identification and the clarification of graphitization degree. Basically, little consideration has been given to combining Raman microscopy and SEM to elucidate the

catalytic mechanism. Such an integration will deepen our understanding of the relationship between morphological changes and phase transitions of catalysts in a catalytic reaction. Therefore, the advantages of this system in characterizing the same microregion of interest in a material have not been fully considered.

Li et al. obtained highly active near-infrared photocatalysts with core-shell structure by etching SrO-Bi₂O₃-B₂O₃ glass-ceramic (GC) samples with hydrochloric acid and *in situ* forming BiOCl nanosheets on the remaining CG cores.⁶⁰ The system was used for microregion analysis, and the peak shapes of Raman spectra were different due to the different vibration modes of chemical bonds, facilitating for probing the phase structure of BiOCl and CG. Then, Raman imaging was used to visually describe the distribution of the two, as shown in Figure 5B. It can be distinguished that the green part of the GC15 surface belongs to BiOCl and that the red part in the middle attributes to the GC structure by the Raman characteristics. According to the strength of the Raman peak, the remaining CG structure after hydrochloric acid etching has a low phonon energy of 248 cm⁻¹, which is conducive to producing high-efficiency up-conversion luminescence.

In 2022, Liu et al. demonstrated the successful preparation of Ti₂CT_x MXene quantum dots by using the RISE technique, X-ray photoelectron spectroscopy, and Fourier transform infrared spectroscopy.⁶¹ Feng et al. constructed a chainmail catalyst (Co-NC-AD, where AD presents post-adsorption process) with excellent stability through a competitive complexation and post-adsorption strategy and analyzed the degree of graphitization of carbon support using RISE microscopy, proving that the addition of metal nanoparticles can promote the formation of a graphitic carbon structure at high temperature, thus explaining the reason for the increase of the overall conductivity of the catalyst.⁶² Similarly, Song and Zhou et al. also analyzed the degree of graphitization of carbon support in ZnCo-NC and FeCu-NC catalysts using the technique.^{63,64}

The application in environmental science

RISE microscopy also shines in the field of environmental science. Here, we focus on the typical case of studying the release information of microplastics (MPs) and nanoplastics (NPs) by using RISE microscopy.

Although the hyperspectral imaging technique can also obtain 1D spectral information and spatial imaging information of samples, as well as measurement and visualization of MPs and NPs in organisms or an environment, it cannot obtain the information for the NPs with the same plastic background substrate.⁶⁵ Due to the small size of individual nanoparticles and the fact that NPs often exist in the form of heterogeneous aggregates in natural environments, it is difficult to directly analyze their chemical structure using traditional characterization techniques.^{66,67} Raman imaging can be an excellent solution to the aforementioned problems due to its higher imaging resolution than Fourier transform infrared spectroscopy microscopy and thus can effectively analyze and visualize the compositional information of MPs.^{68–70} In 2019, Sobhani et al. successfully identified and visualized MPs from a soil/sand background via Raman imaging.⁷¹ Although Raman imaging can obtain and visualize information on the compositional distribution of MPs, it is limited by the drawbacks of small depth of field and low resolution of a microscope, which prevents high-resolution morphological characterization of a region. Luo et al. first observed the morphology of Teflon-coated non-stick cookware after a mimic cooking by SEM, through which the generation of debris and fine structure (web-wire-particle) both at microsize could be observed. Then, it was confirmed that this cookware

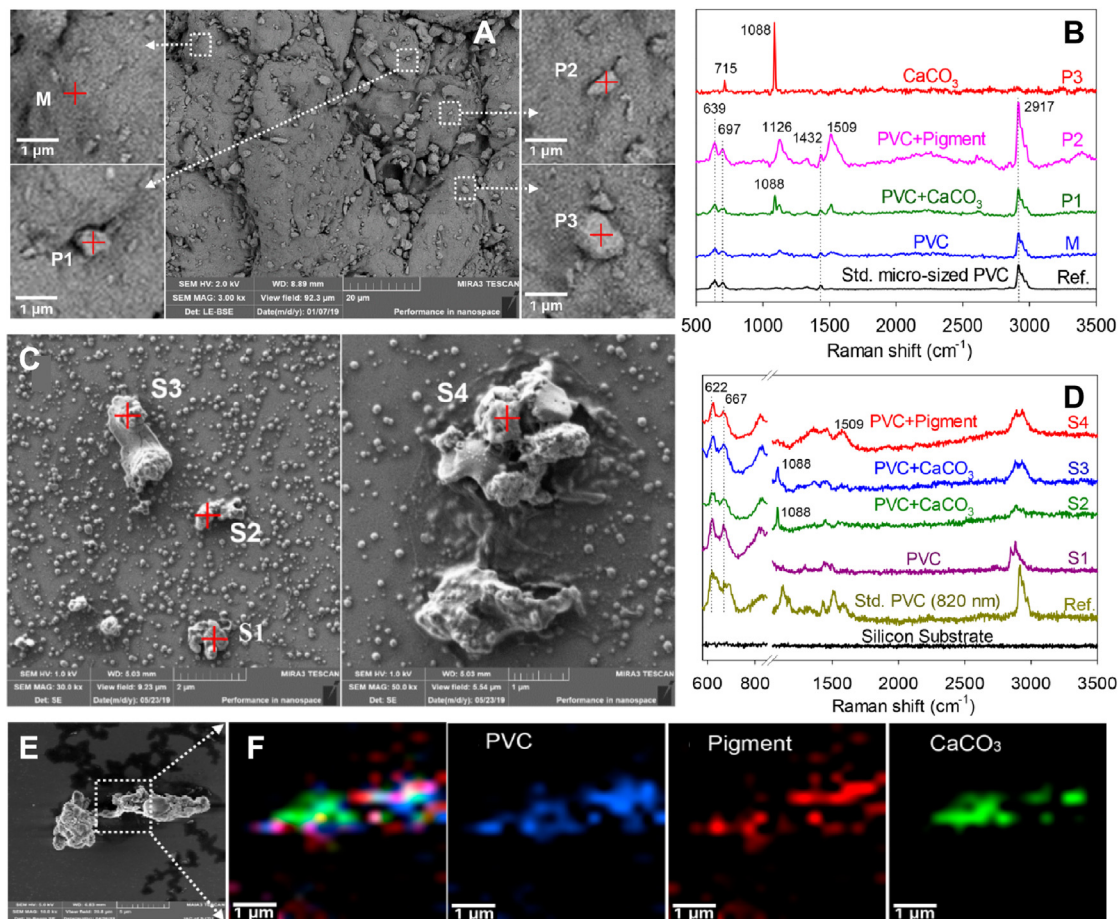


Figure 6. SEM images, Raman spectra, and Raman mapping of NPs on the surface of recycled PVC powders

Reproduced with permission.⁷³ Copyright American Chemical Society, 2020.

- (A) SEM images of the matrix of recycled PVC powders.
- (B) Raman spectra at the marks in (A).
- (C) SEM images of NPs and/or their aggregates.
- (D) Raman spectra at the marks in (C).
- (E) SEM image of a nanosized PVC/pigment/CaCO₃ composite.
- (F) Raman mapping of NPs released from recycled PVC powder, where blue, red, and green represent PVC, pigment, and CaCO₃, respectively.

generates plastic contaminants during the cooking process via Raman imaging.⁷² It is interesting for the study of MPs and NPs if SEM and Raman characterization of the same region can be performed in a microscope. In this way, one can observe the morphology of a sample by using SEM and then analyze the chemical structure of the specified morphology region via Raman microscopy.

The invention of RISE microscopy certainly fulfills this vision. With RISE microscopy, one can easily acquire images from SEM and employ Raman point-to-particle to identify the targets where information on the release of NPs from the plastic recycling process can be easily obtained without separating or destroying the sample. In 2020, Zhang et al. directly identified the chemical information of NPs on the surface of polyvinyl chloride (PVC) powder through RISE microscopy, providing direct evidence for the release of NPs in a plastic recycling process.⁷³ Comparing Figures 6A and 6B with Figures 6C and 6D, it can be found that PVC and/or corresponding aggregates are released from the surface during the recycling process

of recycled PVC powders. The detailed procedures are as follows: select a $5 \times 5 \mu\text{m}$ region of interest in the window of the Raman optical microscope, set specific imaging parameters, and then click to collect scanning imaging data. The region consists of 20×20 pixels resulting in 400 Raman spectra. After the collection of hyperspectral datasets containing the information of hundreds of Raman spectra, the datasets are processed according to the characteristic peaks of PVC (622 and 667 cm^{-1}), pigment ($1,509 \text{ cm}^{-1}$), and CaCO_3 ($1,088 \text{ cm}^{-1}$) by using the RISE software so as to obtain the individual Raman images describing the chemical information of different components in the aggregates. The 2D images of Raman visually show that PVC and pigment are evenly mixed and that their distribution is correlated, while calcium carbonate is relatively concentrated. Thus, it can visually distinguish the three components of PVC, pigment, and calcium carbonate released on the surface during the recycled PVC powders recycling process (Figures 6E and 6F). So, the technique enables us to directly observe the potential release of NPs in the recycling process of commercial PVC plastic materials. As a result, it fills the gap in our understanding of the chemical information of single-particle NPs and is of great significance for analyzing the decomposition of NPs. Raman spectroscopy has great potential for the fields of MPs due to its unique characterization advantages. By combining morphological and elemental analyses, it can further deepen the understanding of MP degradation. Dong et al. studied weathered MPs in natural environments by using RISE microscopy. With the assistance of Fourier transform infrared spectrometry and EDS characterization techniques, they built a preliminary Raman database of weathered MPs containing 124 Raman spectra of weathered MPs. As a consequence, it enables the possible accurate identification of MPs in natural environments.⁷⁴

The applications in miscellaneous fields

In addition to its extensive applications in the fields of energy storage, catalysis, and environmental science, RISE microscopy has also revealed its powerful utilization in other miscellaneous fields. Here, we mainly include some representative works.

Since its debut in 2014, RISE microscopy has been widely used in thin-film coating and composite materials. In 2019, Chu et al. made an in-depth research of the microstructure of $\text{YBa}_2\text{Cu}_3\text{O}_{7-\delta}$ (YBCO) film on CeO_2 substrate after quenching in the early stage of nucleation with the assistance of the hyphenate, as shown in Figures 7A and 7B.⁷⁵ Although there are differences in the morphology of YBCO, the phase composition and grain growth direction are similar, which gives us an insight into the nucleation process and growth mechanism of YBCO deposition on CeO_2 basement. Subsequently, Zhu et al. analyzed the relationship among crystallinity, stress, and crack of yttria-stabilized zirconia (YSZ) coating by combining it with electron backscattered diffraction.⁷⁶ Through SEM images, it can be observed that there are some pores and cracks in YSZ coating (Figure 7C), but it is difficult to obtain the internal relationship between crack generation and stress. It can be found, by comparing the half-peak width and Raman band shift of green and yellow spectra, that the crystallinity of the green region is superior to that of the yellow region and that the tensile stress is less than that of the yellow region (Figure 7E). From Figures 7C–7E, it can be visualized that the yellow region is mainly distributed near the crack and that the region has poor crystallinity and larger tensile stress, being more prone to crack generation. In 2021, You et al. also explored the transformation mechanism of brushite (DCPD) precursor coating into octacalcium phosphate (OCP) and hydroxyapatite (HA) during the initial hydrothermal process by RISE microscopy.⁷⁷ In Figures 7F and 7G, the red area is DCPD and the blue area belongs to OCP/HA, displaying the relative distribution of DCPD and OCP/HA in the coating. That is, DCPD mainly distributes in

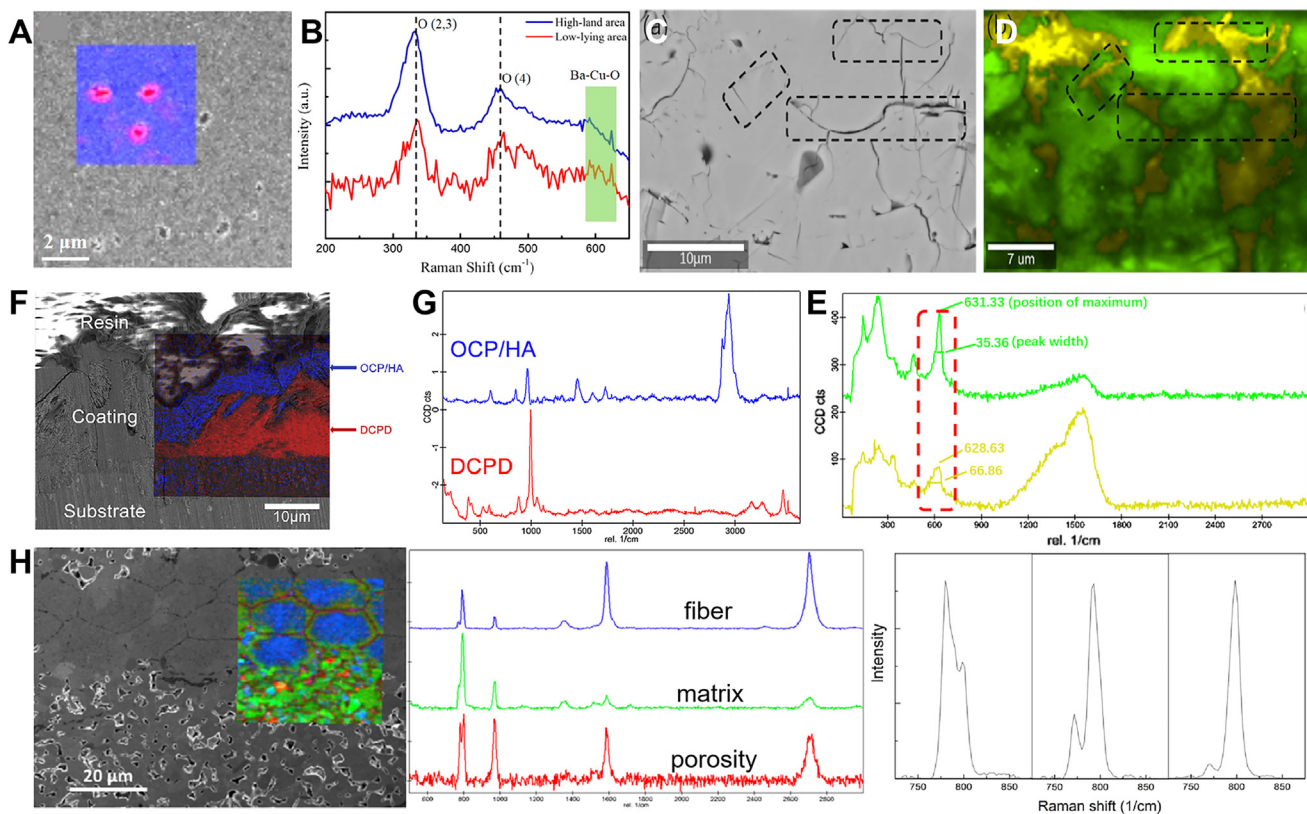


Figure 7. SEM images, Raman spectra, and RISE imaging of thin-film coating and composite materials

(A) RISE imaging of selected region of YBCO film indicating high-land areas (blue) and low-lying areas (red). Reproduced with permission.⁷⁵ Copyright American Chemical Society, 2019.

(B) Raman spectra extracted from cluster analysis for high-land area (blue) and low-lying area (red). Reproduced with permission.⁷⁵ Copyright American Chemical Society, 2019.

(C-E) The SEM image, Raman imaging, and Raman spectra of the polishing section of YSZ coating, respectively. Reproduced with permission.⁷⁶ Copyright ASM International, 2020.

(F and G) RISE imaging and Raman spectra of the cross-section area of the HA-20 min coating, respectively. Reproduced with permission.⁷⁷ Copyright Elsevier, 2020.

(H) RISE imaging, Raman spectra of the SiC_f/SiC specimen, and Raman spectra of carbon in unsintered SiC fibers, respectively. Reproduced with permission.⁷⁸ Copyright authors, 2021.

the inner layer and OCP/HA mainly distributes in the outer layer. During the initial hydrothermal process, the outer layer of the DCPD precursor coating is first transformed into OCP and HA, and the transformation is relatively uniform, which can be directly reflected by the hyphenate system.

In 2021, Li et al. analyzed the microscopic distribution of silicon carbide (SiC) fibers and SiC matrix in SiC_f/SiC composites fabricated by the spark plasma sintering method through RISE microscopy, as shown in Figure 7H.⁷⁸ The technique can directly describe the microstructural changes of each component of the composite before and after sintering, which plays a crucial role in assisting the preparation of high-performance materials.

RISE microscopy is also widely used to analyze asbestos fibers in mineral substrates of mineral mixtures.^{79,80} CRM, as an important part of the RISE microscopy system, is not only capable of point, line, and surface analysis, but more importantly, the confocal function allows for 3D Raman volume analysis.^{81,82} This greatly stimulated interest in

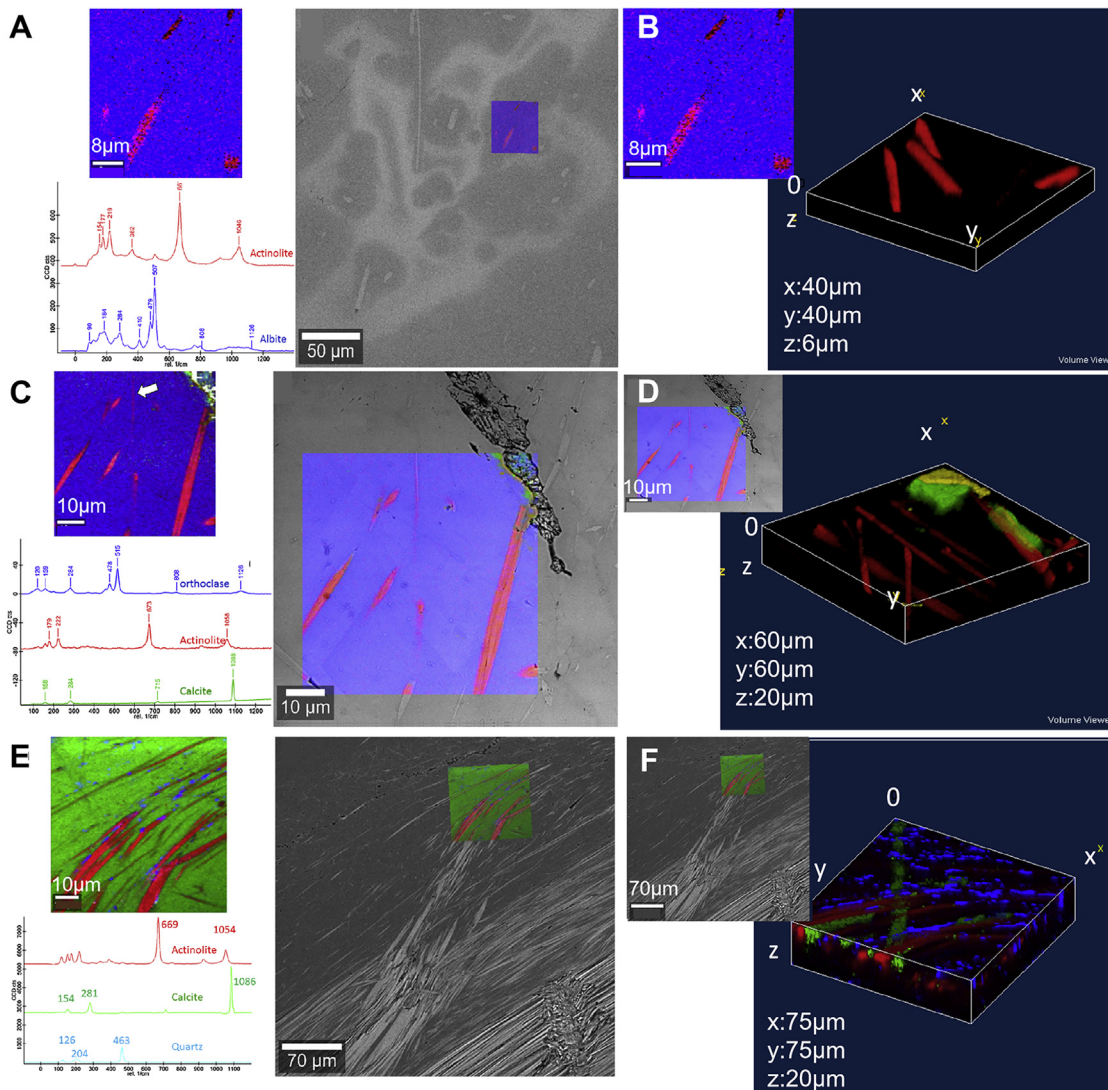


Figure 8. Raman spectra, RISE imaging, and 3D Raman volume analysis of fibrous amphiboles

Reproduced with permission.⁸³ Copyright Elsevier, 2019.

(A, C, and E) RISE imaging and corresponding Raman spectra of samples 1, 2, and 3, respectively.
(B, D, and F) The 3D Raman volume analysis of the areas shown in (A), (C), and (E), respectively.

exploring geological mineral. Wille et al. successfully identified submicron fibers in different mineral substrates and obtained morphological information of amphibolite fibers in volume through RISE microscopy.⁸³ In the selected area of sample 1, the distribution of actinite fibers with fiber diameters ranges from several micrometers to several hundreds of nanometers in the albite matrix, as shown in Figure 8A. In the selected area of sample 2, the distribution of actinite fiber calcite in the orthoclase matrix can be clearly described, as shown in Figure 8C. Likewise, the distribution of fine fibers, calcite particles, and quartz can be clearly described in the selected area of sample 3 (Figure 8E). In order to pinpoint the shape and aspect ratio of the amphibolite and to identify the characteristics of the material containing asbestos, they performed 3D Raman volume analysis, through which the elongation/diameter ratio can be accurately determined. The 3D view of the 2D map analysis area in sample 1 is shown in Figure 8B. In this 3D view, the specific shape of paystone fiber and its real distribution in the matrix can be

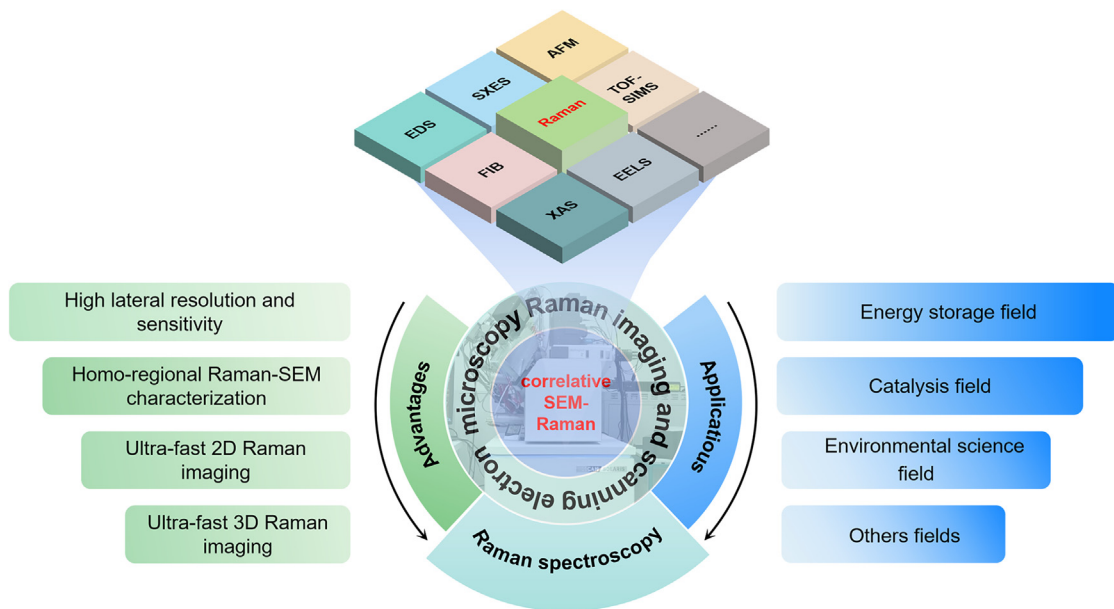


Figure 9. The advantages and applications of RISE microscopy

visualized. In the Raman imaging of sample 2, the actinite fibers observed in the 3D view seem to be elongated, with a high aspect ratio. Through the 3D view, it can be confirmed that the fine fibers observed in the 2D map are fiber bundles, and the thinnest may be asbestos, as shown in [Figure 8D](#). Many fine fibers without preferred orientation can be observed from the 3D view of sample 3. Through 3D Raman imaging, the information below the surface of the sample can also be obtained, further highlighting the advantages of the hyphenate system in material characterization, as shown in [Figure 8F](#).

DISCUSSION

As an emerging advanced spectral analysis method, RISE microscopy has been widely used in energy storage, catalysis, and environmental science as well as in other fields due to its powerful ability of comprehensive analysis in the same region of a sample. The technique combines SEM and Raman microscopy, a mutually beneficial pairing, allowing not only the high-resolution morphological information obtained by SEM but also the chemical and structural analyses of specified areas by Raman. More importantly, the distribution of each phase can also be visually described in a 2D image. However, the resolution of conventional Raman microscopy is limited by the size of the laser beam spot, which makes it difficult to reach the theoretical diffraction limit. Interestingly, RISE microscopy not only has an optical objective with a high numerical aperture to focus the laser beam spot but can also perform the imaging through the scanning motion of a beam spot, which allows for 360 nm lateral resolution (532 nm excitation laser). RISE microscopy is equipped with a Raman microscope with a confocal Raman imaging function, where only the Raman signal from the focal plane is picked up by the detector. The CRM can perform rapidly point, line, and surface analysis, and more importantly, the confocal function also allows for rapid 3D imaging of Raman spectra by scanning layer by layer in three dimensions with an optical objective lens. This minireview summarizes the recent work of the RISE microscopy technique in various research fields ([Figure 9](#)).

Clearly, the hyphenate system is becoming a very important and powerful characterization tool for analyzing material morphology and molecular composition information in

the same microregion. However, apart from the use of this technique for physical characterization, its advantages in coupling with SEM have been generally overlooked in many fields. Herein, we put forward a reasonable prospect. In the field of catalysis research, we mostly use the *in situ* Raman technique to explore the catalytic mechanism dynamically. However, *in situ* Raman can only obtain spectral information and cannot establish the relationship between the surface morphological changes and the kinetics of a catalyst. It is expected that using RISE, one can simultaneously conduct *in situ* dynamic characterization by Raman and high-resolution morphological characterization at the different stages of the catalytic reaction by SEM, so that the understanding of the relationship between the morphological changes and the kinetics of the samples could be deepened. In brief, due to its unique features, RISE microscopy is expected to have a promising future in a wide range of research fields.

ACKNOWLEDGMENTS

This research is supported by the National Natural Science Foundation of China (52272209, 52101256, and 51932003) and the Fundamental Research Funds for the Central Universities JLJ.

AUTHOR CONTRIBUTIONS

F.L. contributed to literature collection, analysis, and manuscript writing. X.Z. provided supervision throughout manuscript writing and financial support. N.Y. contributed to literature collection. W. Zhang contributed to conceptualization, provided supervision throughout manuscript writing, manuscript revising, and financial support. W. Zheng contributed to manuscript revising and financial support. All authors contributed to preparing the manuscript.

DECLARATION OF INTERESTS

The authors declare no competing interests.

REFERENCES

1. Raman, C.V., and Krishnan, K.S. (1928). A New Type of Secondary Radiation. *Nature* 121, 501–502. <https://doi.org/10.1038/121501c0>.
2. Schmidt, U., Ibach, W., Müller, J., Weishaupt, K., and Hollricher, O. (2006). Raman spectral imaging—A nondestructive, high resolution analysis technique for local stress measurements in silicon. *Vib. Spectrosc.* 42, 93–97. <https://doi.org/10.1016/j.vibspec.2006.01.005>.
3. Wermelinger, T., Borgia, C., Solenthaler, C., and Spolenak, R. (2007). 3-D Raman spectroscopy measurements of the symmetry of residual stress fields in plastically deformed sapphire crystals. *Acta Mater.* 55, 4657–4665. <https://doi.org/10.1016/j.actamat.2007.04.036>.
4. Dhakal, K.P., Duong, D.L., Lee, J., Nam, H., Kim, M., Kan, M., Lee, Y.H., and Kim, J. (2014). Confocal absorption spectral imaging of MoS₂: optical transitions depending on the atomic thickness of intrinsic and chemically doped MoS₂. *Nanoscale* 6, 13028–13035. <https://doi.org/10.1039/c4nr03703k>.
5. Levermore, J.M., Smith, T.E.L., Kelly, F.J., and Wright, S.L. (2020). Detection of Microplastics in Ambient Particulate Matter Using Raman Spectral Imaging and Chemometric Analysis. *Anal. Chem.* 92, 8732–8740. <https://doi.org/10.1021/acs.analchem.9b05445>.
6. Hubble, H.W., Kudryashov, I., Solozhenko, V.L., Zinin, P.V., Sharma, S.K., and Ming, L.C. (2004). Raman studies of cubic BC₂N, a new superhard phase. *J. Raman Spectrosc.* 35, 822–825. <https://doi.org/10.1002/jrs.1205>.
7. Zheng, Y., Deng, T., Yue, N., Zhang, W., Zhu, X., Yang, H., Chu, X., and Zheng, W. (2021). Raman spectroscopy and correlative-Raman technology excel as an optimal stage for carbon-based electrode materials in electrochemical energy storage. *J. Raman Spectrosc.* 52, 2119–2130. <https://doi.org/10.1002/jrs.6178>.
8. Dieing, T., and Hollricher, O. (2008). High-resolution, high-speed confocal Raman imaging. *Vib. Spectrosc.* 48, 22–27. <https://doi.org/10.1016/j.vibspec.2008.03.004>.
9. Wachs, I.E. (1999). *In situ* Raman spectroscopy studies of catalysts. *Top. Catal.* 8, 57–63. <https://doi.org/10.1023/A:1019100925300>.
10. Hu, X., Li, Z., and Chen, J. (2017). Flexible Li-CO₂ Batteries with Liquid-Free Electrolyte. *Angew. Chem., Int. Ed. Engl.* 56, 5785–5789. <https://doi.org/10.1002/anie.201701928>.
11. Yang, C., Chen, J., Ji, X., Pollard, T.P., Lü, X., Sun, C.J., Hou, S., Liu, Q., Liu, C., Qing, T., et al. (2019). Aqueous Li-ion battery enabled by halogen conversion-intercalation chemistry in graphite. *Nature* 569, 245–250. <https://doi.org/10.1038/s41586-019-1175-6>.
12. Yan, Z., Sun, H., Chen, X., Liu, H., Zhao, Y., Li, H., Xie, W., Cheng, F., and Chen, J. (2018). Anion insertion enhanced electrodeposition of robust metal hydroxide/oxide electrodes for oxygen evolution. *Nat. Commun.* 9, 2373. <https://doi.org/10.1038/s41467-018-04788-3>.
13. Vecera, P., Chacón-Torres, J.C., Pichler, T., Reich, S., Soni, H.R., Görling, A., Edelthalhammer, K., Peterlik, H., Hauke, F., and Hirsch, A. (2017). Precise determination of graphene functionalization by *in situ* Raman spectroscopy. *Nat. Commun.* 8, 15192. <https://doi.org/10.1038/ncomms15192>.
14. Stöckle, R.M., Suh, Y.D., Deckert, V., and Zenobi, R. (2000). Nanoscale chemical analysis by tip-enhanced Raman spectroscopy. *Chem. Phys. Lett.* 318, 131–136. [https://doi.org/10.1016/S0009-2614\(99\)01451-7](https://doi.org/10.1016/S0009-2614(99)01451-7).
15. Verma, P. (2017). Tip-Enhanced Raman Spectroscopy: Technique and Recent Advances. *Chem. Rev.* 117, 6447–6466. <https://doi.org/10.1021/acs.chemrev.6b00821>.
16. Stiles, P.L., Dieringer, J.A., Shah, N.C., and Van Duyne, R.P. (2008). Surface-enhanced Raman spectroscopy. *Annu. Rev. Anal. Chem.* 1,

- 601–626. <https://doi.org/10.1146/annurev.chem.1.031207.112814>.
17. Clark, R.J.H., and Dines, T.J. (1986). Resonance Raman Spectroscopy, and Its Application to Inorganic Chemistry. New Analytical Methods (27. Angew. Chem., Int. Ed. Engl. 25, 131–158. <https://doi.org/10.1002/anie.198601311>.
18. Sauer, G.R., Zunic, W.B., Durig, J.R., and Wuthier, R.E. (1994). Fourier Transform Raman Spectroscopy of Synthetic and Biological Calcium Phosphates. *Calcif. Tissue Int.* 54, 414–420. <https://doi.org/10.1007/BF00305529>.
19. Aoki, N., Omachi, A., Uosaki, K., and Kondo, T. (2016). Structural Study of Electrochemically Lithiated Si (111) by using Soft X-ray Emission Spectroscopy Combined with Scanning Electron Microscopy and through X-ray Diffraction Measurements. *Chemelectrochem* 3, 959–965. <https://doi.org/10.1002/celc.201600030>.
20. Terauchi, M., Koshiya, S., Satoh, F., Takahashi, H., Handa, N., Murano, T., Koike, M., Imazono, T., Koeda, M., Nagano, T., et al. (2014). Chemical state information of bulk specimens obtained by SEM-based soft-X-ray emission spectrometry. *Microsc. Microanal.* 20, 692–697. <https://doi.org/10.1017/S1431927614000439>.
21. Zhou, X., Qiao, S., Yue, N., Zhang, W., and Zheng, W. (2022). Soft X-ray emission spectroscopy finds plenty of room in exploring lithium-ion batteries. *Mater. Res. Lett.* 11, 239–249. <https://doi.org/10.1080/21663831.2022.2141586>.
22. Zhang, T., Yu, H., Shi, J., Wang, X., Luo, H., Lin, D., Liu, Z., Su, C., Wang, Y., and Liu, L. (2022). Correlative AFM and Scanning Microlens Microscopy for Time-Efficient Multiscale Imaging. *Adv. Sci.* 9, e2103902. <https://doi.org/10.1002/advs.202103902>.
23. Wirth, R. (2009). Focused Ion Beam (FIB) combined with SEM and TEM: Advanced analytical tools for studies of chemical composition, microstructure and crystal structure in geomaterials on a nanometre scale. *Chem. Geol.* 261, 217–229. <https://doi.org/10.1016/j.chemgeo.2008.05.019>.
24. Weigel, A.V., Chang, C.-L., Shtengel, G., Xu, C.S., Hoffman, D.P., Freeman, M., Iyer, N., Aaron, J., Khuon, S., Bogovic, J., et al. (2021). ER-to-Golgi protein delivery through an interwoven, tubular network extending from ER. *Cell* 184, 2412–2429.e16. <https://doi.org/10.1016/j.cell.2021.03.035>.
25. Tian, R., Duan, H., Guo, Y., Li, H., and Liu, H. (2018). High-Coulombic-Efficiency Carbon/Li Clusters Composite Anode without Precycling or Prelithiation. *Small* 14, 1802226. <https://doi.org/10.1002/smll.201802226>.
26. Sun, C., Zhao, B., Mao, J., Dai, K.H., Wang, Z.y., Tang, L.b., Chen, H.z., Zhang, X.h., and Zheng, J.c. (2023). Enhanced Cycling Stability of 4.6 V LiCoO₂ Cathodes by Inhibiting Catalytic Activity of its Interface Via MXene Modification. *Adv. Funct. Mater.* 33, 2300589. <https://doi.org/10.1002/adfm.202300589>.
27. Hollricher, O., Schmidt, U., and Breuninger, S. (2014). RISE Microscopy: Correlative Raman-SEM Imaging. *Microsc. Today* 22, 36–39. <https://doi.org/10.1017/s1551929514001175>.
28. Jones, R.R., Hooper, D.C., Zhang, L., Wolverson, D., and Valev, V.K. (2019). Raman Techniques: Fundamentals and Frontiers. *Nanoscale Res. Lett.* 14, 231. <https://doi.org/10.1186/s11671-019-3039-2>.
29. Loudon, R. (1964). The Raman effect in crystals. *Adv. Phys. X* 13, 423–482. <https://doi.org/10.1080/00018736400101051>.
30. Das, R.S., and Agrawal, Y.K. (2011). Raman spectroscopy: Recent advancements, techniques and applications. *Vib. Spectrosc.* 57, 163–176. <https://doi.org/10.1016/j.vibspec.2011.08.003>.
31. Wille, G., Bourrat, X., Maubec, N., and Lahfid, A. (2014). Raman-in-SEM, a multimodal and multiscale analytical tool: performance for materials and expertise. *Micron* 67, 50–64. <https://doi.org/10.1016/j.micron.2014.06.008>.
32. Krishnan, R.S., and Shankar, R.K. (1981). Raman effect: History of the discovery. *J. Raman Spectrosc.* 10, 1–8. <https://doi.org/10.1002/jrs.1250100103>.
33. van Apeldoorn, A.A., Aksенov, Y., Stigter, M., Hofland, I., de Brujin, J.D., Koerten, H.K., Otto, C., Greve, J., and van Blitterswijk, C.A. (2005). Parallel high-resolution confocal Raman SEM analysis of inorganic and organic bone matrix constituents. *J. R. Soc., Interface 2*, 39–45. <https://doi.org/10.1098/rsif.2004.0018>.
34. Cardell, C., and Guerra, I. (2016). An overview of emerging hyphenated SEM-EDX and Raman spectroscopy systems: Applications in life, environmental and materials sciences. *TrAC Trends Anal. Chem.* 77, 156–166. <https://doi.org/10.1016/j.trac.2015.12.001>.
35. Timmermans, F.J., and Otto, C. (2015). Contributed Review: Review of integrated correlative light and electron microscopy. *Rev. Sci. Instrum.* 86, 011501–12112. <https://doi.org/10.1063/1.4905434>.
36. Aksenov, Y.Y., Reinders, E.G.I., Greve, J., van Blitterswijk, C., de Brujin, J., and Otto, C. (2000). Integration of a confocal Raman microscope in an electron microscope. *Laser Microscopy* 4164, 90–96. <https://doi.org/10.1117/12.410628>.
37. Aksenov, Y., van Apeldoorn, A.A., de Brujin, J.D., Blitterswijk, C.v., Greve, J., and Otto, C. (2002). Combined Confocal Raman Microscope with Scanning Electron Microscope; A Parallel Analysis of Inorganic and Organic Materials. *Microsc. Microanal.* 8, 1386–1387. <https://doi.org/10.1017/s1431927602103047>.
38. Williams, K., Bennett, R., Brooker, A., Bormett, R., and Prusnick, T. (2003). New Methods in Raman Spectroscopy—Combining Other Microscopes. *Microsc. Microanal.* 9, 1094–1095. <https://doi.org/10.1017/s1431927603445479>.
39. Hazekamp, J., Reed, M.G., Howard, C.V., VAN Apeldoorn, A.A., and Otto, C. (2011). The feasibility of Cryo In-SEM Raman microspectroscopy. *J. Microsc.* 244, 122–128. <https://doi.org/10.1111/j.1365-2818.2011.03515.x>.
40. Schmidt, R., Fitzek, H., Nachtnebel, M., Mayrhofer, C., Schroettner, H., and Zankel, A. (2019). The Combination of Electron Microscopy, Raman Microscopy and Energy Dispersive X-Ray Spectroscopy for the Investigation of Polymeric Materials. *Macromol. Symp.* 384, 1800237. <https://doi.org/10.1002/masy.201800237>.
41. Jiruse, J., Hanicinec, M., Havelka, M., Hollricher, O., Ibach, W., and Spizig, P. (2014). FIB-SEM Instrument with Integrated Raman Spectroscopy for Correlative Microscopy. *Microsc. Microanal.* 20, 990–991. <https://doi.org/10.1017/s1431927614006679>.
42. Yang, B., Zhang, W., and Zheng, W. (2023). Unlocking the full energy densities of carbon-based supercapacitors. *Mater. Res. Lett.* 11, 517–546. <https://doi.org/10.1080/21663831.2023.2183783>.
43. Zhao, Z., Zhang, W., Liu, M., Wang, D., Wang, X., Zheng, L., Zou, X., Wang, Z., Li, D., Huang, K., and Zheng, W. (2023). Switching Optimally Balanced Fe–N Interaction Enables Extremely Stable Energy Storage. *Energy Environ. Mater.* 6, e12342. <https://doi.org/10.1002/eem2.12342>.
44. Zhao, Z., Zhang, W., Liu, M., Yoo, S.J., Yue, N., Liu, F., Zhou, X., Song, K., Kim, J.-G., Chen, Z., et al. (2023). Ultrafast Nucleation Reverses Dissolution of Transition Metal Ions for Robust Aqueous Batteries. *Nano Lett.* 23, 5307–5316. <https://doi.org/10.1021/acs.nanolett.3c01435>.
45. Zheng, Y., Deng, T., Zhang, W., and Zheng, W. (2020). Optimizing the micropore-to-mesopore ratio of carbon-fiber-cloth creates record-high specific capacitance. *J. Energy Chem.* 47, 210–216. <https://doi.org/10.1016/j.jechem.2019.12.014>.
46. Zandiashbar, A., Lee, G.H., An, S.J., Lee, S., Mathew, N., Terrones, M., Hayashi, T., Picu, C.R., Hone, J., and Koratkar, N. (2014). Effect of defects on the intrinsic strength and stiffness of graphene. *Nat. Commun.* 5, 3186. <https://doi.org/10.1038/ncomms4186>.
47. Li, D., Zhao, L., Cao, X., Xiao, Z., Nan, H., and Qiu, H. (2021). Nickel-catalyzed formation of mesoporous carbon structure promoted capacitive performance of exhausted biochar. *Chem. Eng. J.* 406, 126856. <https://doi.org/10.1016/j.cej.2020.126856>.
48. Huang, C., Wang, D., Zhang, W., Yoo, S.J., Zhou, X., Song, K., Chen, Z., Zou, X., Yue, N., Wang, Z., et al. (2022). Substitution-triggered broken symmetry of cobalt tungstate boosts redox kinetics in pseudocapacitive storage. *Cell Rep. Phys. Sci.* 3, 101115. <https://doi.org/10.1016/j.xrpp.2022.101115>.
49. Wang, W.-N., Meng, D., Qian, G., Xie, S., Shen, Y., Chen, L., Li, X., Rao, Q., Che, H., Liu, J., et al. (2020). Controlling Particle Size and Phase Purity of “Single-Crystal” LiNi_{0.5}Mn_{1.5}O₄ in Molten-Salt-Assisted Synthesis. *J. Phys. Chem. C* 124, 27937–27945. <https://doi.org/10.1021/acs.jpcc.0c09313>.
50. Pasero, D., Reeves, N., Pralong, V., and West, A.R. (2008). Oxygen Nonstoichiometry and Phase Transitions in LiMn_{1.5}Ni_{0.5}O_{4-δ}. *J. Electrochem. Soc.* 155, A282. <https://doi.org/10.1149/1.2832650>.
51. Wang, L., Li, H., Huang, X., and Baudrin, E. (2011). A comparative study of Fd-3m and P4₃21 “LiNi_{0.5}Mn_{1.5}O₄”. *Solid State Ionics* 193, 32–38. <https://doi.org/10.1016/j.ssi.2011.04.007>.

52. Cabana, J., Casas-Cabanas, M., Omenya, F.O., Chernova, N.A., Zeng, D., Whittingham, M.S., and Grey, C.P. (2012). Composition-structure relationships in the Li-ion battery electrode material $\text{LiNi}_{0.5}\text{Mn}_{1.5}\text{O}_4$. *Chem. Mater.* 24, 2952–2964. <https://doi.org/10.1021/cm301148d>.
53. Cai, L., Liu, Z., An, K., and Liang, C. (2013). Unraveling structural evolution of $\text{LiNi}_{0.5}\text{Mn}_{1.5}\text{O}_4$ by *in situ* neutron diffraction. *J. Mater. Chem. A* 1, 6908–6914. <https://doi.org/10.1039/c3ta00145h>.
54. Jehnichen, P., and Korte, C. (2019). Operando Raman Spectroscopy Measurements of a High-Voltage Cathode Material for Lithium-Ion Batteries. *Anal. Chem.* 91, 8054–8061. <https://doi.org/10.1021/acs.analchem.8b05819>.
55. Qian, G., Monaco, F., Meng, D., Lee, S.-J., Zan, G., Li, J., Karpov, D., Gul, S., Vine, D., Stripe, B., et al. (2021). The role of structural defects in commercial lithium-ion batteries. *Cell Rep. Phys. Sci.* 2, 100554. <https://doi.org/10.1016/j.xcrp.2021.100554>.
56. Li, J., Zhang, W., Ge, X., Lu, M., Xue, X., Wang, Z., Yue, N., Zhang, J., Lang, X., Jiang, Q., and Zheng, W. (2022). Etching-courtesy NH_4^+ pre-intercalation enables highly-efficient Li^+ storage of MXenes via the renaissance of interlayer redox. *J. Energy Chem.* 72, 26–32. <https://doi.org/10.1016/j.jechem.2022.04.030>.
57. Sun, Y., Wang, H., Meng, D., Li, X., Liao, X., Che, H., Cui, G., Yu, F., Yang, W., Li, L., and Ma, Z.-F. (2021). Degradation Mechanism of O3-Type $\text{NaNi}_{1/3}\text{Fe}_{1/3}\text{Mn}_{1/3}\text{O}_2$ Cathode Materials During Ambient Storage and Their In Situ Regeneration. *ACS Appl. Energy Mater.* 4, 2061–2067. <https://doi.org/10.1021/acs.ame.4c00047>.
58. Pan, Z., Qin, T., Zhang, W., Chu, X., Dong, T., Yue, N., Wang, Z., and Zheng, W. (2022). Non-layer-transformed Mn_2O_4 cathode unlocks optimal aqueous magnesium-ion storage via synergizing amorphous ion channels and grain refinement. *J. Energy Chem.* 68, 42–48. <https://doi.org/10.1016/j.jechem.2021.11.031>.
59. Yang, H., Qin, T., Zhou, X., Feng, Y., Wang, Z., Ge, X., Yue, N., Li, D., Zhang, W., and Zheng, W. (2022). Boosting the kinetics of PF_6^- into graphitic layers for the optimal cathode of dual-ion batteries: the rehearsals of pre-intercalating Li^+ . *J. Energy Chem.* 71, 392–399. <https://doi.org/10.1016/j.jechem.2022.04.009>.
60. Li, G., Huang, S., Yuan, H., Zhu, N., and Wei, Y. (2020). Efficient and regenerative near-infrared glass-ceramic photocatalyst fabricated by a facile *in-situ* etching method. *Chem. Eng. J.* 394, 124877. <https://doi.org/10.1016/j.cej.2020.124877>.
61. Liu, Y., Zhang, X., Zhang, W., Ge, X., Wang, Y., Zou, X., Zhou, X., and Zheng, W. (2022). MXene-Based Quantum Dots Optimize Hydrogen Production via Spontaneous Evolution of Cl- to O-Terminated Surface Groups. *Energy Environ. Mater.* e12438 <https://doi.org/10.1002/eem.2.12438>.
62. Feng, Y., Song, K., Zhang, W., Zhou, X., Yoo, S.J., Kim, J.-G., Qiao, S., Qi, Y., Zou, X., Chen, Z., et al. (2022). Efficient ORR catalysts for zinc-air battery: Biomass-derived ultra-stable Co nanoparticles wrapped with graphitic layers via optimizing electron transfer. *J. Energy Chem.* 70, 211–218. <https://doi.org/10.1016/j.jechem.2022.01.047>.
63. Zhou, X., Song, K., Feng, Y., Jiang, C., Chen, Z., Wang, Z., Yue, N., Ge, X., Zhang, W., and Zheng, W. (2023). Individually-atomic governing d– π^* orbital interactions via Cu-promoted optimization of Fe-d band centers for high-efficiency zinc-air battery. *Nano Res.* 16, 4634–4642. <https://doi.org/10.1007/s12274-022-5091-y>.
64. Song, K., Feng, Y., Zhou, X., Qin, T., Zou, X., Qi, Y., Chen, Z., Rao, J., Wang, Z., Yue, N., et al. (2022). Exploiting the trade-offs of electron transfer in MOF-derived single Zn/Co atomic couples for performance-enhanced zinc-air battery. *Appl. Catal., B* 316, 121591. <https://doi.org/10.1016/j.apcatb.2022.121591>.
65. Zhang, Y., Wang, X., Shan, J., Zhao, J., Zhang, W., Liu, L., and Wu, F. (2019). Hyperspectral Imaging Based Method for Rapid Detection of Microplastics in the Intestinal Tracts of Fish. *Environ. Sci. Technol.* 53, 5151–5158. <https://doi.org/10.1021/acs.est.8b07321>.
66. Schwaferts, C., Niessner, R., Elsner, M., and Ivleva, N.P. (2019). Methods for the analysis of submicrometer- and nanoplastic particles in the environment. *TrAC Trends Anal. Chem.* (Reference Ed.) 112, 52–65. <https://doi.org/10.1016/j.trac.2018.12.014>.
67. Nguyen, B., Claveau-Mallet, D., Hernandez, L.M., Xu, E.G., Farmer, J.M., and Tufenkji, N. (2019). Separation and Analysis of Microplastics and Nanoplastics in Complex Environmental Samples. *Acc. Chem. Res.* 52, 858–866. <https://doi.org/10.1021/acs.accounts.8b00602>.
68. Luo, Y., Gibson, C.T., Chuah, C., Tang, Y., Ruan, Y., Naidu, R., and Fang, C. (2022). Fire releases micro- and nanoplastics: Raman imaging on burned disposable gloves. *Environ. Pollut.* 312, 120073. <https://doi.org/10.1016/j.envpol.2022.120073>.
69. Fang, C., Luo, Y., and Naidu, R. (2023). Microplastics and nanoplastics analysis: Options, imaging, advancements and challenges. *TrAC Trends Anal. Chem.* (Reference Ed.) 166, 117158. <https://doi.org/10.1016/j.trac.2023.117158>.
70. Luo, Y., Awoyemi, O.S., Naidu, R., and Fang, C. (2023). Detection of microplastics and nanoplastics released from a kitchen blender using Raman imaging. *J. Hazard Mater.* 453, 131403. <https://doi.org/10.1016/j.jhazmat.2023.131403>.
71. Sobhani, Z., Al Amin, M., Naidu, R., Megharaj, M., and Fang, C. (2019). Identification and visualisation of microplastics by Raman mapping. *Anal. Chim. Acta* 1077, 191–199. <https://doi.org/10.1016/j.aca.2019.05.021>.
72. Luo, Y., Gibson, C.T., Chuah, C., Tang, Y., Naidu, R., and Fang, C. (2022). Raman imaging for the identification of Teflon microplastics and nanoplastics released from non-stick cookware. *Sci. Total Environ.* 851, 158293. <https://doi.org/10.1016/j.scitotenv.2022.158293>.
73. Zhang, W., Dong, Z., Zhu, L., Hou, Y., and Qiu, Y. (2020). Direct Observation of the Release of Nanoplastics from Commercially Recycled Plastics with Correlative Raman Imaging and Scanning Electron Microscopy. *ACS Nano* 14, 7920–7926. <https://doi.org/10.1021/acsnano.0c02878>.
74. Dong, M., Zhang, Q., Xing, X., Chen, W., She, Z., and Luo, Z. (2020). Raman spectra and surface changes of microplastics weathered under natural environments. *Sci. Total Environ.* 739, 139990. <https://doi.org/10.1016/j.scitotenv.2020.139990>.
75. Chu, J., Zhao, Y., Khan, M.Z., Tang, X., Wu, W., Shi, J., Wu, Y., Huhtinen, H., Suo, H., and Jin, Z. (2019). Insight into the Interfacial Nucleation and Competitive Growth of $\text{YBa}_2\text{Cu}_3\text{O}_{7-\delta}$ Films as High-Performance Coated Conductors by a Fluorine-Free Metal–Organic Decomposition Route. *Cryst. Growth Des.* 19, 6752–6762. <https://doi.org/10.1021/acs.cgd.9b01120>.
76. Zhu, X., Huang, Y., Zheng, W., Zhang, J., Lin, C., Schwalb, C., and Zeng, Y. (2020). Crystallinity, Stresses, and Cracks of YSZ Coatings Characterized by SEM–EBSD–Raman Spectroscopy. *J. Therm. Spray Technol.* 29, 995–1001. <https://doi.org/10.1007/s11666-020-01051-4>.
77. You, M., Echeverry-Rendón, M., Zhang, L., Niu, J., Zhang, J., Pei, J., and Yuan, G. (2021). Effects of composition and hierarchical structures of calcium phosphate coating on the corrosion resistance and osteoblast compatibility of Mg alloys. *Mat. Sci. Eng. C-Mater* 120, 111734. <https://doi.org/10.1016/j.msec.2020.111734>.
78. Li, K., Kashkarov, E., Ma, H., Fan, P., Zhang, Q., Zhang, P., Zhang, J., Wu, Z., Wahl, L., Laptev, R., et al. (2021). Microstructural Analysis of Novel Preceramic Paper-Derived SiC_x/SiC Composites. *Materials* 14, 6737. <https://doi.org/10.3390/ma14226737>.
79. Dong, M., Zhang, Q., Xing, X., Chen, W., She, Z., and Luo, Z. (2020). Raman spectra and surface changes of microplastics weathered under natural environments. *Sci. Total Environ.* 739, 139990. <https://doi.org/10.1016/j.scitotenv.2020.139990>.
80. Liu, D., Yu, N., Papineau, D., Fan, Q., Wang, H., Qiu, X., She, Z., and Luo, G. (2019). The catalytic role of planktonic aerobic heterotrophic bacteria in protodolomite formation: Results from Lake Jibuhulangtu Nuur, Inner Mongolia, China. *Geochim. Cosmochim. Acta* 263, 31–49. <https://doi.org/10.1016/j.gca.2019.07.056>.
81. SWEATMAN, T.R., and LONG, J.V.P. (1969). Quantitative Electron-probe Microanalysis of Rock-forming Minerals. *J. Petrol.* 10, 332–379. <https://doi.org/10.1093/petrology/10.2.332>.
82. McGee, J.J., and Keil, K. (2002). Application of Electron Probe Microanalysis to the Study of Geological and Planetary Materials. *Microsc. Microanal.* 7, 200–210. <https://doi.org/10.1007/s10050010081>.
83. Wille, G., Lahondere, D., Schmidt, U., Duron, J., and Bourrat, X. (2019). Coupling SEM-EDS and confocal Raman-in-SEM imaging: A new method for identification and 3D morphology of asbestos-like fibers in a mineral matrix. *J. Hazard Mater.* 374, 447–458. <https://doi.org/10.1016/j.jhazmat.2019.04.012>.